# Statistical reconstruction-based scatter correction: a new method for 3D PET

Habib Zaidi[1]

*Abstract* - **Accurate scatter correction is one of the major problems facing quantitative 3D PET and many methods have been developed for the purpose of reducing the resultant degradation of image contrast and loss of quantitative accuracy. A new scatter correction method called Statistical Reconstruction-Based Scatter Correction (SRBSC) is proposed in this paper and evaluated using Monte Carlo simulations, experimental phantoms and clinical studies. For accurate modeling, the scatter fraction and scatter response function for uniformly attenuating media are parametrised using Monte Carlo simulations.**

*Key words* - **PET, scatter correction, OSEM, Monte Carlo.**

## I. INTRODUCTION

One of the obstacles to the use of volume imaging PET scanners is the increase in the scatter fraction which influences the sensitivity and represents from 30% to 50% of the data acquired in 3D mode. The inclusion of Compton-scattered events degrade image quality and can seriously reduce diagnostic accuracy. In addition to a decrease in the image contrast, events may also appear in regions of the image where there is no activity (e.g. outside the patient).

Many scatter correction methods attempt to estimate the scatter contamination and then remove it using either subtraction or deconvolution techniques. Some scatter compensation methods incorporate scatter in the transition matrix or point-spread function during iterative reconstruction. It has been shown that this can lead to highly quantitative accuracy (Floyd *et al* 1986) and improved signal-to-noise ratio in the reconstructed images (Beekman *et al* 1997, Hutton and Baccarne 1998). With the advent of faster computers and accelerated iterative reconstruction algorithms, different approaches to scatter compensation are receiving much attention.

## II. SCATTER CORRECTION METHOD

In this paper, a new technique for scatter correction in 3D PET is proposed. Other investigators independently reported a related method for scatter correction in SPECT imaging (Liu *et al* 1999). The principle of the method is based on the hypothesis that the image corresponding to scattered events in the projection data consist of almost low-frequency components of activity distribution and that the low-frequency components will converge faster than the high-frequency ones in successive iterations of statistical reconstruction methods such as the maximum likelihood - expectation maximisation (ML-EM) or its accelerated version, the ordered subsets - expectation maximisation (OSEM).

It has been shown that iterative reconstruction algorithms possess a non-uniform convergence property (Pan and Yagle 1991). That is, low-frequency components of the image tend to be recovered earlier in iterative reconstruction than high-frequency components. The study of convergence properties of the ML-EM algorithm by Fourier analysis revealed clearly its non-uniform frequency response (Tanaka 1987). Moreover, preliminary investigations of inverse Monte Carlo-based reconstruction indicate that the recovery of spatial frequency information is achieved at different numbers of iterations for different spatial frequencies: higher spatial frequencies appear at higher iterations while the lower frequencies (smooth structures) are well defined at early iterations (Floyd *et al* 1986).

In terms of the frequency response, the scatter components of PET projection data tend to be dominated by low-frequency information, though there is some middle- and high-frequency information present. The SRBSC approach takes advantage of this by estimating the scatter component from forward projection of images reconstructed in early iterations of OSEM. The scatter fraction (*SF*) which gives an indication about the expected amount of scatter and the scatter response function (*srf*) which defines the spatial distribution of scatter in the photopeak data are usually the two parameters required for estimation of scatter component and need to be determined a priori. A pure additive model of the imaging system is assumed here where the recorded data are composed of an unscattered and a scattered component plus a noise term due to statistical fluctuations, and can be written in the following form:

$$p_o = p_u + p_s + \eta$$

where $p_o$ are the observed data, $p_u$ and $p_s$ are the unscattered and scattered components respectively, and $\eta$ is the noise term. The observed data can be modelled as a convolution of the source distribution with the system response function. The total response function of the scanner can be divided in two response kernels corresponding to the scattered and unscattered components, *srf* and *urf*, respectively. By neglecting statistical noise, the measured data can be related to the true activity distribution, *f* by the convolution relation:

$$p_o = fwdproject(f) \otimes (urf + srf) = p_u + p_s$$

Where $\otimes$ denotes the convolution operator and *fwdproject* is the forward projection operator. Within the limits of our assumptions, the activity distribution, *f*, can be roughly divided in two parts:

$$f = f_L + f_H$$

where $f_L$ denotes the low-frequency image and $f_H$ the high-frequency one. Based on the assumption that the high-frequency components will be smeared, i.e. filtered by the scatter response kernels, the scatter component in the projection data can be approximated as follows:

$$p_s = \left[ fwdproject(f_L) + fwdproject(f_H) \right] \otimes srf$$
$$\approx fwdproject(f_L) \otimes srf$$

The proposed SRBSC method for scatter correction exploits the properties mentioned above. The basic steps followed when applying the method consist of the following:

(i) estimate the low-frequency components by only one OSEM iteration;
(ii) obtain the scatter components by forward projection of the estimated image convolved with Monte Carlo simulated scatter response kernel *srf*;
(iii) subtract the estimated scatter components from measured projections;
(iv) reconstruct the image using any available reconstruction algorithm (analytic, iterative) using scatter corrected projection data.

### III. PARAMETRIZATION OF THE SCATTER RESPONSE KERNELS

*Scatter distribution functions.* Fig. 1 shows scatter distribution functions for a simulated line source located at the centre of the FOV (left) and displaced 5 cm radially off-centre (right). It can be seen that the projections of a line source placed in a uniform water-filled cylinder are dominated in the wings by the object scatter and in the peak by the unscattered photons. As expected, the object scatter is fairly well described by monoexponential functions. A linear regression analysis on the wings of the log plot of the projection data was used to estimate the slope, $\alpha$ (in units of cm$^{-1}$). The data in the extreme bins of the projection were excluded to avoid edge effects.
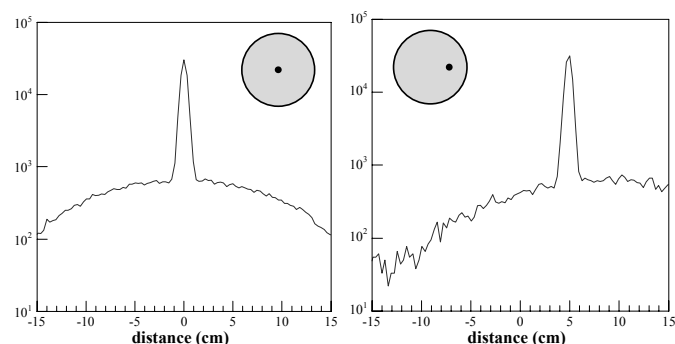


**Fig. 1.** Illustration of the scatter response functions when the line source is located at the centre of the FOV (left) and displaced 5 cm radially (right). The projections for the line source at the centre are symmetrical and were summed over all projection angles.

This discussion remains valid, when the line source is shifted out of the symmetry centre. The amplitude of the short side of the projection compared to that of the symmetrical case is increased, since the path length of the photons through the phantom becomes shorter, whereas the amplitude of the long side is decreased, due to a longer pathway through the attenuating medium. The wings of the scatter distribution functions are still well parametrised by mono-exponentials, but with different parameters for the left and the right side.

For the case when the line source is located at the centre of the cylinder, Table 1 shows a progressive increase in the slope of the scatter function from 0.037 cm$^{-1}$ to 0.099 cm$^{-1}$ with increasing lower energy threshold (LET). This is consistent with the fact that the scatter tails are less pronounced when the LET is increased. A good agreement between measured and simulated data was observed except for a LET setting of 250 keV.

**TABLE I.** Simulated and measured values of $\alpha$ (in cm$^{-1}$), the slope of the scatter function *exp(-αr)* for different lower energy window settings obtained by linear regression analysis.

| LET setting (keV) | simulated $\alpha$ (cm$^{-1}$) | measured $\alpha$ (cm$^{-1}$) |
|---|---|---|
| 250 | 0.037 | 0.051 ± 0.005 |
| 300 | 0.049 | 0.055 ± 0.005 |
| 350 | 0.064 | 0.067 ± 0.006 |
| 380 | 0.084 | 0.081 ± 0.007 |
| 400 | 0.099 | - |

*Scatter fraction.* The scatter fraction was examined with respect to three parameters: (i) variation in lower energy threshold setting, (ii) variation in radial position of the line source within the cylindrical phantom, and (iii) variation in the diameter of the cylindrical phantom. The variation of the *SF* was investigated in the same way as the scatter distribution function. However, in addition to the line source geometry, the variation of the scatter fraction in a uniform cylindrical phantom as a function of its size and for three lower energy thresholds (250, 380 and 450 keV) was also studied. The scatter fraction is estimated directly from the results of the Monte Carlo simulation as the ratio between scattered and total coincidences (Zaidi *et al* 1999). To fit the data, a simple function was derived *SF(R)=1-exp(-2kR)*. As reported by Adam *et al* (1996), this function fits the scatter fraction of a uniform activity distribution in cylindrical phantoms as well as centred and off-centred line sources reasonably well, although some crude simplifying assumptions have been made for the derivation of this function.
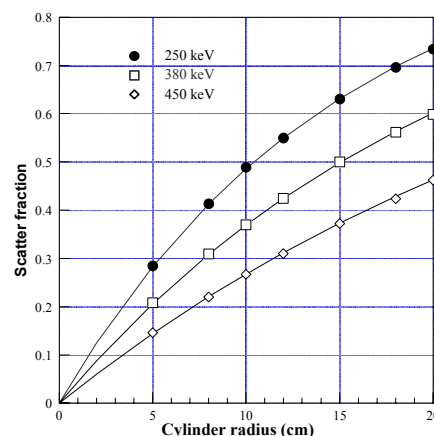


**Fig. 2.** Monte Carlo calculations of the variation of the scatter fraction as a function of the radius *R* of the cylindrical phantom for a central line source using three different LET settings. The fitted curves are also shown.

As an example, Fig. 2 illustrates the variation of the *SF* as a function of the radius *R* of the cylinder for a centred line source for the three lower energy thresholds. The fitting curves are also shown. Obviously, *SF(R)* increases with increasing *R*. It was observed that, for the same phantom size, the scatter fraction for a line source is always larger than that for a homogeneously distributed activity. This can be explained as follows. For a line source, the two annihilation photons must always travel the maximum path length through the phantom, which is not the case for a homogeneously

distributed activity. The activity distribution in cerebral scans can be considered as a mixture of both components. Consequently, its scatter fraction is between the two extremes.

## IV. THE 3D OSEM RECONSTRUCTION SOFTWARE

A software implementation of OSEM was performed using an object-oriented library for 3D PET reconstruction developed within the PARAPET European project (Labbé *et al* 1999). As 3D iterative reconstruction algorithms are time consuming, the library contains classes and functions to run parts of the reconstruction in parallel, using parallel platforms with distributed memory architecture. The algorithm combines the forward and backprojection operators with an appropriate choice of ordered sets to fully use all symmetry properties for fast computation (Jacobson *et al* 1999). An analysis of the convergence properties of OSEM revealed that one iteration of OSEM is sufficient to assess the distribution of low-frequency scatter. This property makes the method very fast, which renders its implementation in clinical routine viable.

## V. PHANTOM SIMULATIONS AND EXPERIMENTAL STUDIES

An evaluation of the relative performance of the proposed method was performed using Monte Carlo simulated data and experimental phantoms of the Utah phantom and the 3D Hoffman brain phantom for the ECAT 953B scanner operated in 3D mode. A calculated attenuation correction was applied to simulated data sets. Transmission data was used instead in the experimental phantoms and clinical studies. The filtered backprojection/reprojection method (3D-RP) of Kinahan and Rogers (1989) was used to reconstruct the data sets.

Well-established metrics are used to assess image quality. This includes calculations of the contrast or relative concentrations measured in the different compartments of the Utah phantom, the signal-to-noise ratio and the recovery coefficient. The signal-to-noise ratio was defined as the mean number of events divided by the standard deviation of pixel intensities in a ROI defined within the background region of the Utah phantom.

The unscattered component in the simulated projection data was recorded and used as a reference to which the scatter corrected projections are compared. Fig. 3 shows a comparison of a profile through a sinogram plane representing the true unscattered component as estimated by the Monte Carlo simulations and by the scatter correction procedure for the Utah phantom. The scatter correction technique gives a reasonable estimation of the scatter component and successfully brings the activity to zero faster outside the object.

The simulated reference image, reconstructed image corresponding to unscattered events only and images reconstructed before (CA) and after applying scatter subtraction using SRBSC are illustrated in fig. 4. The scatter correction technique improves the quality of the images and allows a better definition of the cold cylinder (left small cylinder) compared to the case where only attenuation correction is applied, however, the images appear noisier after scatter subtraction.
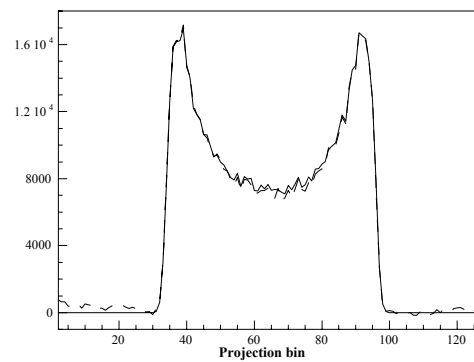


**Fig. 3.** Integral profiles through a sinogram plane of the simulated unscattered component (solid line) and the scatter corrected sinogram using SRBSC (dashed line) for the Utah phantom.
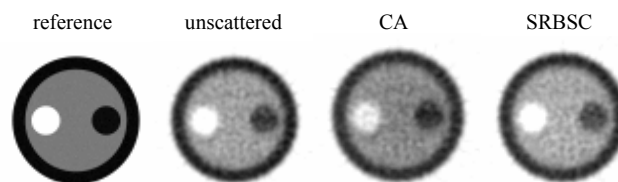


reference　　unscattered　　CA　　SRBSC

**Fig. 4.** Reconstructed images of the simulated Utah phantom.

Table II shows concentration ratios between different compartments of the measured Utah phantom for one distribution of activity before and after 3D attenuation and scatter corrections are performed on the scans. Obviously, the scatter correction method improves the contrast compared to the case where no correction is applied without significantly increasing the noise.

**Table II.** Relative concentrations measured in the different compartments of the scanned Utah phantom without (CA) and with scatter correction (SRBSC). The SNR measured in the background is also shown. The outer compartment (**E**) was filled with activity concentration equal to that in the background region.

| Case | A | B | C | D | SNR |
|---|---|---|---|---|---|
| Calibration concentration | 1 | 1.68 | 2.03 | 0 | - |
| NC | 1 | 1.14 | 1.64 | 0.35 | 20.93 |
| SRBSC | 1 | 1.37 | 1.87 | 0.10 | 18.34 |

Table III shows the results of the quantitative evaluations of the percentage activity recovery in the simulated Hoffman 3D brain phantom before and after applying the scatter correction technique for five circular ROIs, which cover important structures of the brain. The image slice used for calculating the ROIs was the one including the basal ganglia. The SRBSC technique tends to undercorrect for scatter in most regions but gives very good activity recovery values, which average within 4%.

The reconstructed images of the physical 3D Hoffman brain phantom without and with scatter correction are shown in fig. 5. The effect of scatter removal in areas where no activity is present (e.g. CSF) is clearly seen and the contrast between grey and white matter is improved and the structures are more clearly delineated.

**Table III.** Percentage recovery calculated in different structures of clinical interest in the Hoffman 3D brain phantom before (CA) and after applying the scatter correction technique (SRBSC). The average and standard deviation (s.d.) are also shown.

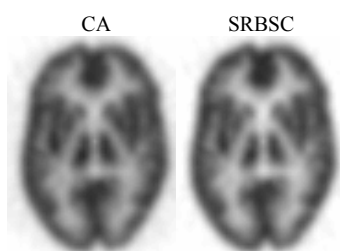|  | Recovery (%) | |
| --- | --- | --- |
| Structure | CA | SRBSC |
| Frontal gyrus | 185.4 | 113.8 |
| White matter | 108.2 | 102.5 |
| CSF | 124.6 | 105.2 |
| Right thalamus | 114.6 | 99.2 |
| Left median temporal gyrus | 108.7 | 99.3 |
| Average | 128.3 | 104.0 |
| s.d. | 32.6 | 6.0 |

CA          SRBSC



**Fig. 5.** Reconstructed images of the physical 3D brain phantom.

## VI. CLINICAL STUDIES

The proposed scatter correction algorithm was also tested on clinical data. Cerebral and oncology clinical studies were selected from the database and used for clinical evaluation of the scatter correction method. Fig. 6 illustrates a slice from the uncorrected and scatter corrected 3D clinical study at the level of the thorax. It should be noted that for the whole-body, it is difficult to assess the effect of the scatter correction in the images shown. However, the streak artefacts seen in the attenuation corrected image only have been significantly reduced after scatter subtraction.
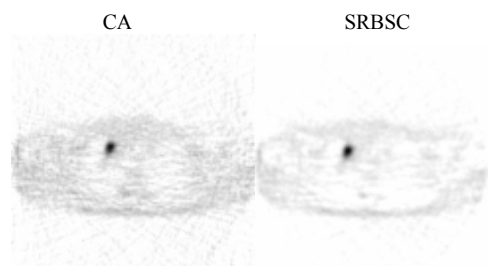
CA                    SRBSC



**Figure 6.** Reconstructed images of an oncology study.

## VII. DISCUSSION AND CONCLUSIONS

In summary, we have developed a new scatter correction method for fully 3D PET imaging. The SRBSC approach is computationally efficient as it can be easily implemented on vector or parallel computing hardware and the software required either for forward projection or fast Fourier transform is widely available in the public domain. Moreover, the low spatial frequency nature of the scatter distribution allows reducing the data size by coarse rebinning in the radial and axial direction without sacrificing the accuracy in the scatter

distribution estimation. Completion of the proposed SRBSC algorithm for scatter correction by including accurate models for detector efficiency, multiple scatters, scatter from outside the field-of-view and a number of minor improvements would enable quantitative, fully 3D PET imaging in the head and the body. We believe that the basic principles of the method could also be applied to other scanner geometries including dual-head coincidence imaging and the combined PET/CT system, as well as to other imaging modalities such as transmission CT and the combined SPECT/CT. However, the success of such applications will depend on the efficient and accurate calculation of scatter responses from objects with non-uniform density.

### REFERENCES

Adam L E, Bellemann M E, Brix G, Lorenz W J 1996 Monte Carlo-based analysis of PET scatter components. J. Nucl. Med. **37** 2024-2029

Bailey D L and Meikle S R 1994 A convolution-subtraction scatter correction method for 3D PET Phys. Med. Biol. **39** 411-424

Beekman F J, Kamphuis C and Frey E C 1997 Scatter correction methods in 3D iterative SPECT reconstruction: A simulation study. Phys. Med. Biol. **42** 1619-1631

Floyd C E, Jaszczak R J, Greer K L, Coleman R E 1986 Inverse Monte Carlo as a unified reconstruction algorithm for ECT. J. Nucl. Med. **27** 1577-1585

Hutton B F and Baccarne V 1998 Efficient scatter modelling for incorporation in maximum likelihood reconstruction. Eur J Nucl Med. **25** 1658-1665

Jacobson M, Levkovitz R, Ben-Tal A, *et al* 1999 Enhanced 3D PET OSEM reconstruction using iterative filtering. *submitted to* Phys. Med. Biol.

Kinahan P E and Rogers J G 1989 Analytic 3D image reconstruction using all detected events. IEEE Trans. Nucl. Sci. **36** 964-968

Labbé C, Thielemans K, Zaidi H, Morel C 1999 An object-oriented library incorporating efficient projector/backprojector operators for 3D PET reconstruction. *Proc.* of the International Meeting on Fully Three-dimensional Image Reconstruction in Radiology and Nuclear Medicine (3D'99), Egmond aan Zee, Netherlands 23-26 June 1999, pp 137-140

Liu Z, Obi T, Yamaguchi M and Ohyama N 1999 Fast estimation of scatter components using the ordered subsets expectation maximization algorithm for scatter compensation. Opt. Rev. **6** 415-423

Pan T S and Yagle A E 1991 Numerical study of multigrid implementations of some iterative image reconstruction algorithms. IEEE Trans. Med. Imag. **10** 572-588

Tanaka E 1987 A fast reconstruction algorithm for stationary positron emission tomography based on a modified EM algorithm. IEEE Trans. Med. Imag. **6** 98-105

Zaidi H, Herrmann Scheurer A, and Morel C 1999 An object-oriented Monte Carlo simulator for 3D positron tomographs. Comput. Methods Programs Biomed. **58** 133-145

[1] Geneva University Hospital, Division of Nuclear Medicine, Switzerland habib.zaidi@hcuge.ch